Solid Freeform Fabrication 2023: Proceedings of the 34th Annual International Solid Freeform Fabrication Symposium – An Additive Manufacturing Conference
Reviewed Paper

Microstructure and Mechanical Properties of Additively Manufactured Haynes 282: A Comparative Analysis between Laser Powder Bed Fusion and Laser Powder Directed Energy Deposition Technologies

Nabeel Ahmad[1,2], Reza Ghiaasiaan[1,2], Paul R. Gradl[3], Shuai Shao[1,2], Nima Shamsaei[1,2*]

[1] National Center for Additive Manufacturing Excellence (NCAME), Auburn University, Auburn, AL 36849, USA

[2] Department of Mechanical Engineering, Auburn University, Auburn, AL36849, USA

[3] NASA Marshall Space Flight Center, Propulsion Department, Huntsville, AL 35812, USA

*Corresponding author: shamsaei@auburn.edu

Phone: (334) 844-4839

Abstract

This study compares the microstructure and tensile properties of Haynes 282 fabricated using laser powder bed fusion and laser powder directed energy deposition. Both sets underwent stress-relieving, followed by hot isostatic pressing, and the standard double aging heat treatment. Tensile testing was conducted at room temperature on specimens fabricated with both technologies to evaluate and compare their tensile behaviors. Results show that the ultimate tensile and yield strengths of laser powder bed fused specimens were 18% and 57% higher, respectively than those of laser powder directed energy deposited ones, whereas the elongation to failure was similar in both. The difference in strengths is attributed to the differences in the size of γ' precipitates and grains, i.e., those in the laser powder directed energy deposited specimens being larger, whereas similar elongation to failure is attributed to the carbide debonding dominating the fracture mechanism in both batches.

Keywords: Additive manufacturing; laser powder bed fusion (L-PBF); laser powder directed energy deposition (LP-DED); Haynes 282; grain size; tensile properties

Introduction

Haynes 282 is a nickel-base superalloy, which is known for its excellent strength, decent weldability, and high hardness. A major fraction of its strength is due to γ' precipitates [1,2]. This alloy is often used in aerospace applications such as in gas turbines, where intricate and complex geometries are often required, posing challenges to traditional manufacturing processes (i.e., forging or casting). Moreover, machining this alloy is difficult due to its high hardness and wear resistance [2]. Additive manufacturing (AM) offers a viable solution by fabricating near net shape geometries with complex features and allows the consolidation of assemblies into monolithic parts, potentially reducing cost, lead time, and material waste [3]. Among various AM technologies, laser powder bed fusion (L-PBF) and laser powder directed energy deposition (LP-DED) are widely used [4]. L-PBF uses a laser to selectively melt powder that is uniformly distributed on the build plate. On the other hand, LP-DED technology involves injecting metal powder through a nozzle into a laser beam under controlled atmospheric conditions [5].

Although AM offers several advantages compared to conventional manufacturing, the resulting parts often exhibit variability in their mechanical performance primarily due to heterogeneous microstructure and the presence of volumetric defects, making qualification and certification of parts challenging [6]. Moreover, different AM technologies including L-PBF and LP-DED employ different process parameters, leading to significantly different microstructures and mechanical properties [7–9]. These inherent differences may persist even if similar heat treatment (HT) schedules are applied [10,11]. While several studies investigated the microstructure and mechanical properties of AM Haynes 282 [1,12–15], there is a lack of knowledge regarding the effect of the manufacturing process on the microstructure and mechanical properties. This study examined the

effect of additive manufacturing processes on the microstructural response and resulting mechanical properties of L-PBF and LP-DED Haynes 282.

Experimental Procedure

The chemical compositions of the two powder batches used for fabrication were measured using inductively coupled plasma spectroscopy and presented in **Table 1**. LP-DED specimens were vertically fabricated as cylindrical bars using the RPM Innovations 557 Laser Deposition system, whereas L-PBF specimens were vertically manufactured in near-net shape using an EOS M400 machine. The process parameters employed for manufacturing are shown in **Table 2**.

Table 1. Chemical composition (wt.%) of the powder batches used for fabrication.

Elements	L-PBF	LP-DED
Ni	Bal.	Bal.
Cr	19.7	19.2
Co	10.2	10.2
Mo	8.6	8.4
Ti	2.2	2.2
Al	1.6	1.6
Fe	0.1	0.1
C	0.05	0.04
B	0.008	0.004
Mn	<0.1	<0.1
Si	<0.02	0.05

Table 2. The process parameters used in L-PBF and LP-DED machines for the fabrication of Haynes 282 specimens.

Process	Power (W)	Track thickness (µm)	Travel speed (mm/s)	Powder feed rate (g/min)
L-PBF	285	40	960	---
LP-DED	1070	381	16.93	16.5

Prior to tensile testing, the specimens underwent four-stage HT which involved (1) stress relief (SR) at 1066°C for 1.5 hr followed by furnace cooling to room temperature, then (2) hot isostatic pressing (HIP) at 1165°C for 3 hr at 103 MPa, then (3) solution annealing (SA) at 1135°C for 1 hr and argon quenched to room temperature, and finally (4) double aging (DA) at 1010°C for 2 hr and furnace cooled to 788°C for 8 hr and then argon quenched to room temperature. A schematic illustration of the multi-step HT is also shown in **Figure 2**. After full HT, the cylindrical bars and near-net shape geometries were machined to the tensile geometry, following the dimensions specified in ASTM E8 standard [16].

The coupons were prepared for scanning electron microscopy (SEM) by mounting them on cold epoxy resin and polishing the surfaces to eliminate any scratches. Microstructural analysis was performed on the radial plane (i.e., the plane perpendicular to the build direction) of small coupons excised from the tensile specimens. SEM was conducted using a Zeiss 550 scanning electron microscope equipped with electron backscatter diffraction (EBSD) and energy dispersive X-ray spectroscopy (EDS) detectors. EBSD maps were utilized to analyze the grain size, while electron contrast channeling imaging technique was used to generate backscattered electron (BSE) micrographs.

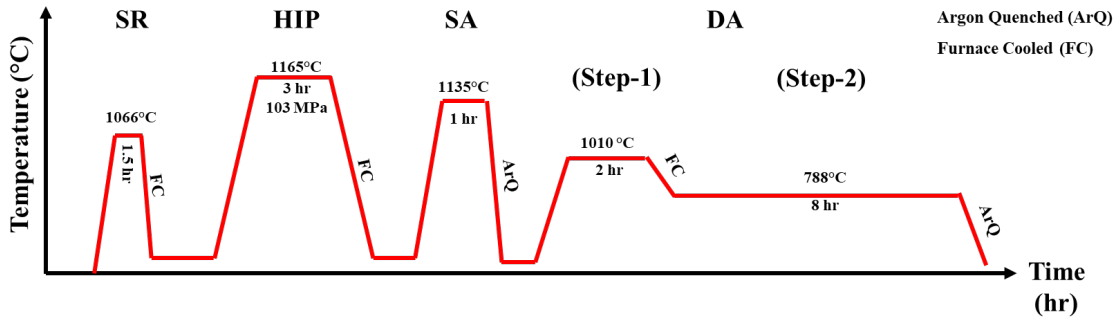

Figure 1. A schematic illustration of the standard HT schedule used for this study for both L-PBF and LP-DED Haynes 282 specimens.

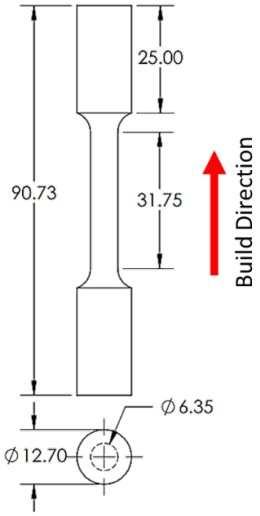

Figure 2. The geometry of tensile test specimens used in this study. All the dimensions are in mm.

Tensile testing was conducted at a strain rate of 0.005 mm/mm/min following the ASTM E8 standard [17] on the fully heat treated (HT) and machined specimens. During testing, the extensometer was detached at a strain value of 0.015 due to its limited travel, and then the test was continued till fracture. At least three specimens were tested at room temperature for both batches and their average values were reported.

Results and Discussion

The inverse pole figure (IPF) maps obtained from the radial plane of both L-PBF and LP-DED specimens in non-heat treated (NHT) and fully HT (i.e., SR+HIP+SA+DA) conditions are shown in **Figure 3**. In NHT condition (see **Figures 3(a) & (c)**), the majority fraction of grains in LP-DED samples exceeded 100 µm, while in L-PBF, it was predominantly below 100 µm (**Figure 3(e)**). After full HT, both batches showed partial recrystallization and the presence of annealing twins (see **Figures 3(b) & (d)**). Moreover, the overall grain size distribution was similar to NHT condition in both the L-PBF and LP-DED samples; LP-DED samples had a predominant fraction of grains larger than 100 µm, whereas L-PBF samples showed the majority fraction below 100 µm (see **Figure 3(f)**). In addition, HT significantly affected smaller grains in LP-DED samples, leading to significant size changes compared to L-PBF samples (see **Figures 3(d) &(f)**).

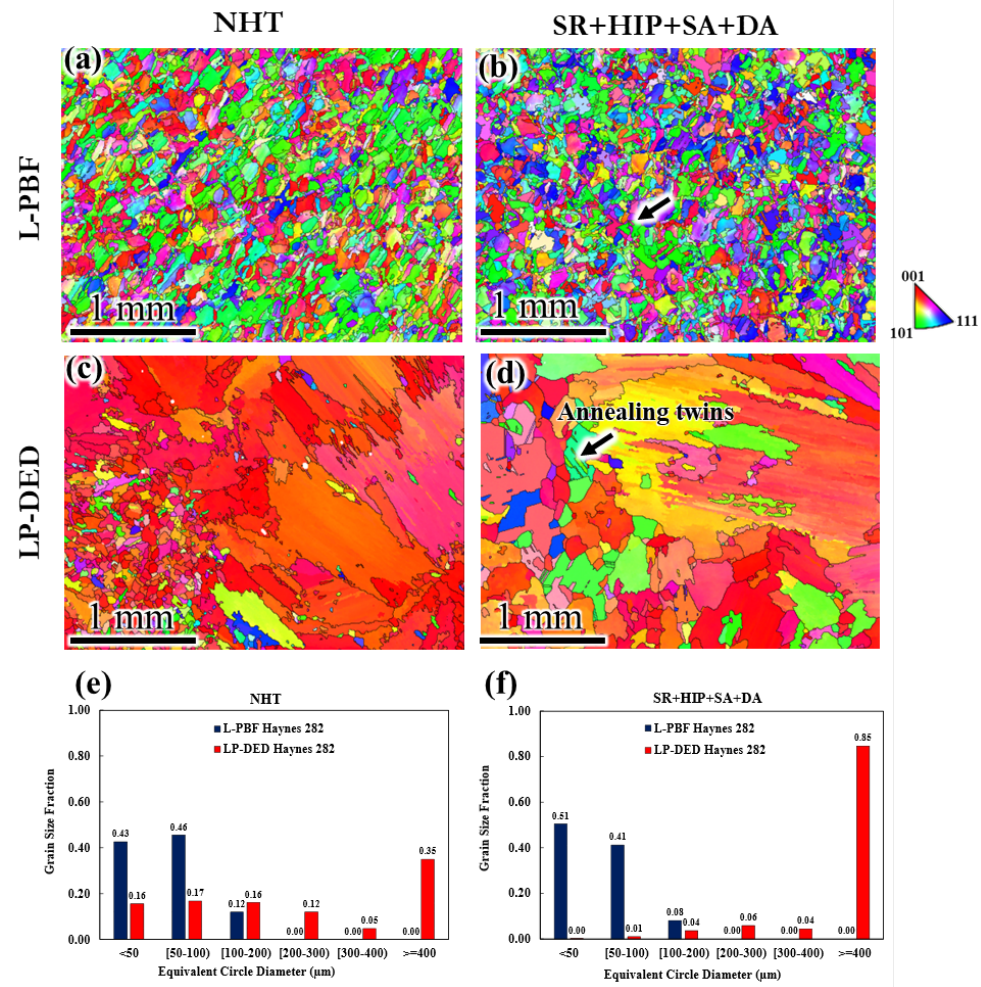

Figure 3. IPF maps taken from the radial plane of L-PBF and LP-DED samples in (a) & (c) NHT and (b) & (d) SR+HIP+SA+DA conditions. (e) and (f) exhibit the grain size distribution in NHT and fully HT conditions, respectively.

The BSE images of NHT and fully HT DED samples are shown in **Figures 4(a) & (c)** and **Figures 4(b) & (d)**, respectively. The NHT condition of both L-PBF and LP-DED specimens exhibited dendritic microstructure. The dendrites were finer in L-PBF samples compared with LP-DED ones, possibly due to the higher solidification rates during L-PBF process [12,18]. Upon full HT, the dendritic microstructure was partially dissolved and grain boundary carbides as well as γ' precipitates were formed. The γ' precipitates present in L-PBF specimens were finer with spherical morphologies (~60±19 nm), while in LP-DED samples they were significantly larger (~263±64 nm) with irregular shapes. The difference in size and mass between L-PBF and LP-DED specimens before machining explains this phenomenon. Due to their larger size and mass, LP-DED specimens likely experienced reduced cooling rates during the multi-step heat treatment, resulting in the formation of coarser precipitates through the Ostwald ripening mechanism [1]. This mechanism favors the growth of larger particles at the expense of smaller ones. The grain boundary particles were analyzed using EDS (see **Figure 5**), which showed these carbides were enriched with Al, Ti, and Mo and they were identified as M_6C and $M_{23}C_6$ type carbides. In addition, Al, Ti, and Ni enrichment at the grain boundaries suggests the presence of γ' precipitates.

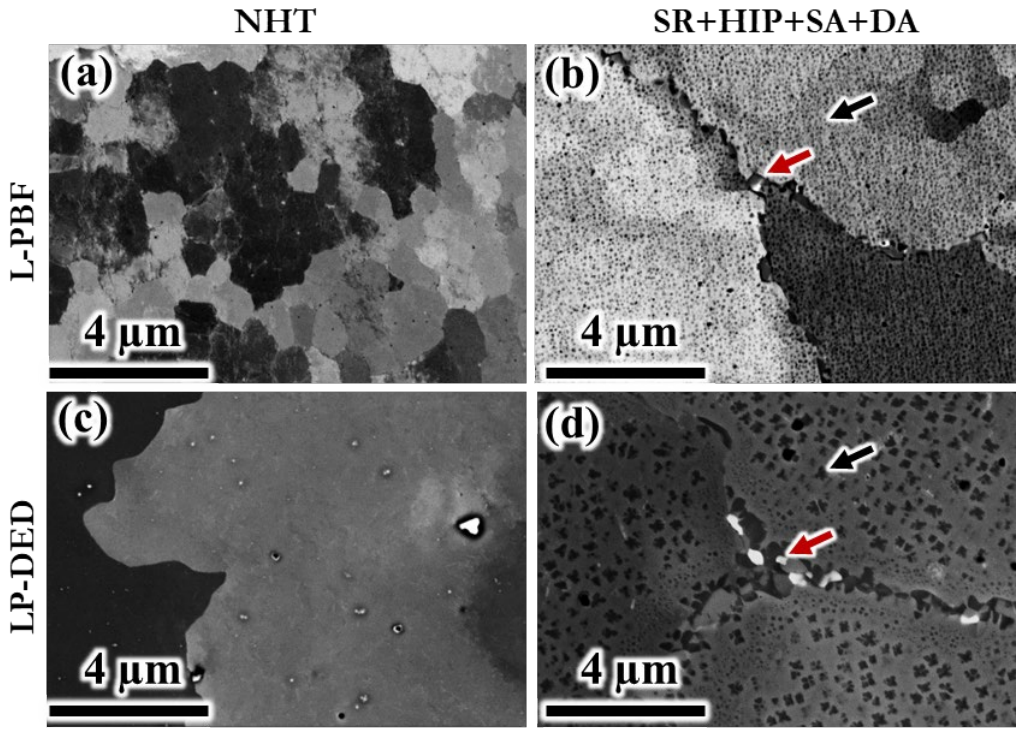

Figure 4. BSE micrographs taken from the radial plane of L-PBF and LP-DED samples in (a) & (c) NHT and (b) & (d) SR+HIP+SA+DA condition. The black and red arrows indicate γ' precipitates and metal carbides, respectively.

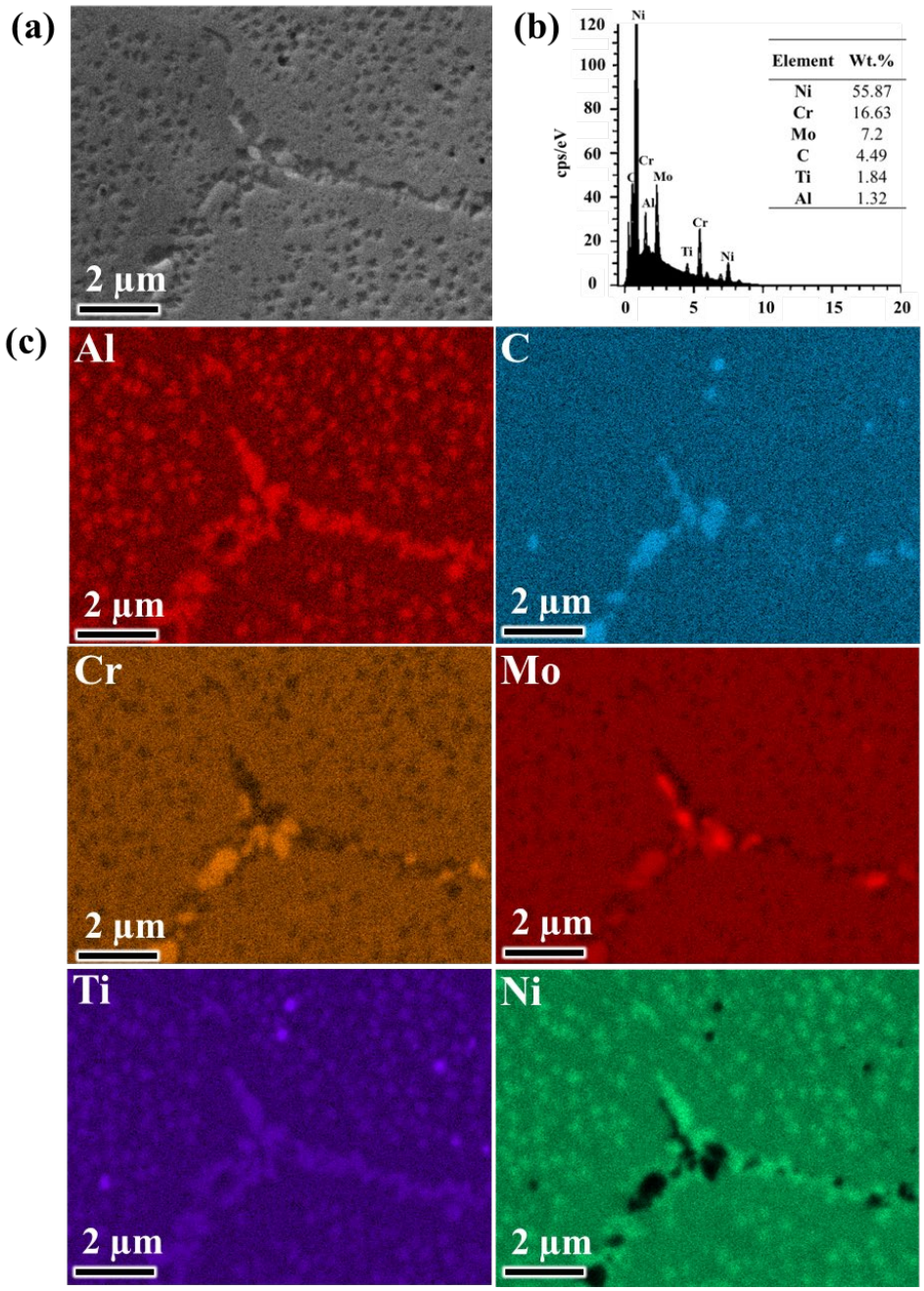

Figure 5. EDS of the fully HT LP-DED Haynes 282 sample: (a) BSE image, (b) X-ray spectrum, (c) elemental maps.

Engineering stress-strain curves of the fully HT and machined L-PBF and LP-DED Haynes 282 specimens are shown in **Figure 6**. Moreover, tensile properties including yield strength (YS), ultimate tensile strength (UTS), and elongation to failure (EL) of both batches are compared with the wrought counterparts (see **Figure 6(b)**). As shown, the L-PBF Haynes 282 exhibited 57% and 18% higher YS and UTS compared to LP-DED specimens. Moreover, the L-PBF Haynes 282 specimens showed 23% and 5% better YS and UTS compared to the wrought counterparts. Interestingly, EL was similar in all manufacturing conditions. A higher tensile strength of L-PBF specimens compared to LP-DED ones can be ascribed to smaller grain size and finer γ' precipitate (see **Figure 3** and **Figure 4**) compared to LP-DED specimens. Since the principal source of strength in Haynes 282 is the ordered γ' precipitates, variations in grain size due to different thermal histories and process parameter should be less pronounced [2]. Similar EL in both LP-DED and L-PBF specimens could be attributed to the similar fracture mechanism, in which carbides debonding from the matrix occurred at the onset of plastic deformation. These deboned carbide particles were found inside the dimples (see **Figure 7(b)**). Similar observations were made in Ref. [1,7,10,19].

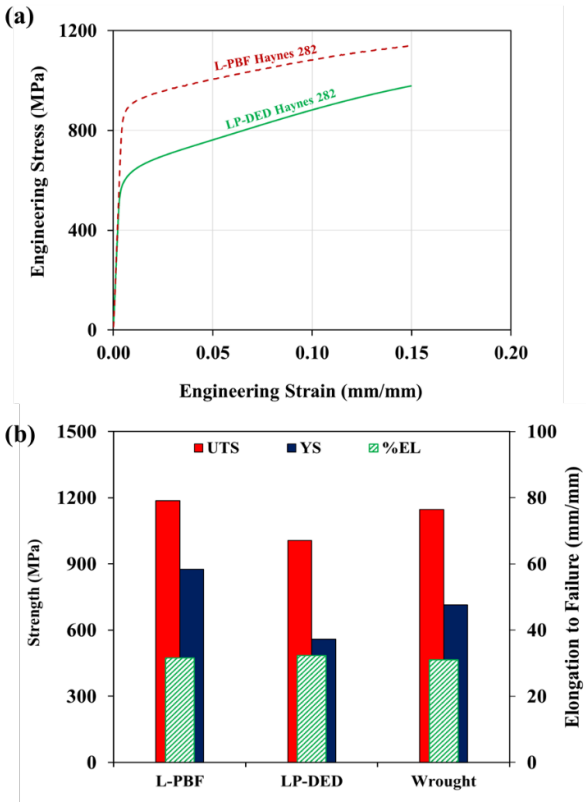

Figure 6. Tensile behavior of LP-DED and L-PBF Haynes 282 specimens: (a) engineering stress-strain curves (b) comparison of tensile properties among different processing methods [20].

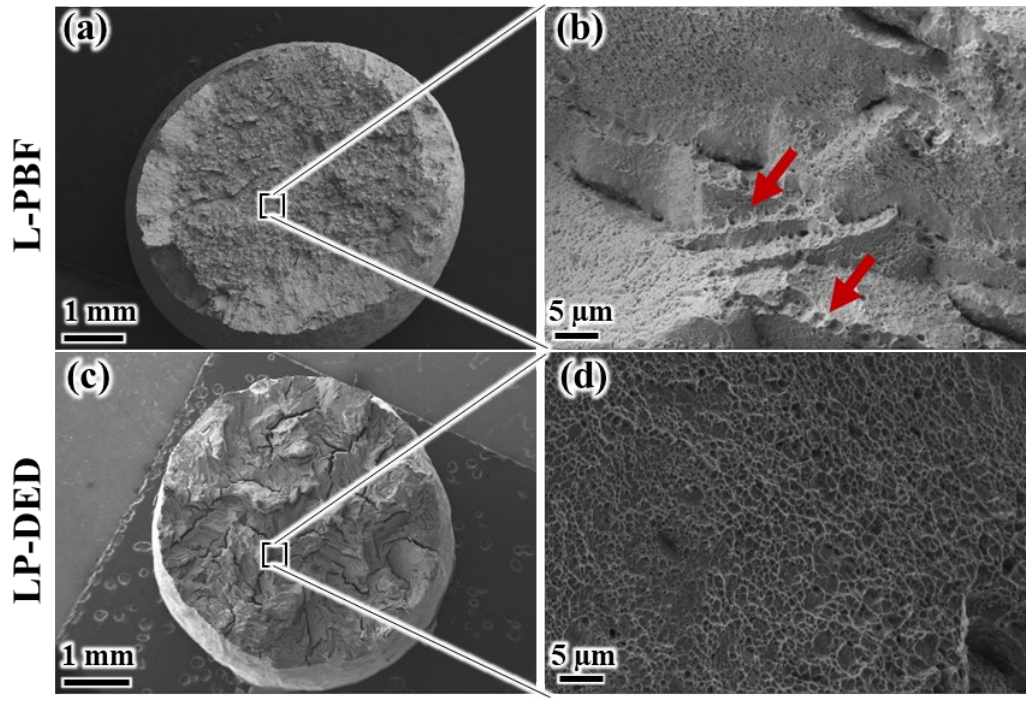

Figure 7. Tensile fracture surfaces of (a)-(b) L-PBF and (c)-(d) LP-DED specimens. The red arrow indicates the fractured particles inside the dimples.

Conclusions

This study compared the effect of a similar heat treatment (HT) schedule on the microstructure and tensile properties of Haynes 282 fabricated using two different additive manufacturing processes, namely, laser powder bed fusion and laser powder directed energy deposition. The following conclusions were drawn:

1) The non-heat treated condition in both batches showed dendritic microstructure, which was partially dissolved into γ matrix following full HT in both the LP-DED and L-PBF specimens.
2) The grain size in L-PBF samples in both non-heat treated and heat treated condition was consistently smaller than in LP-DED samples.
3) After full HT, partial recrystallization occurred in both sets. Moreover, laser powder bed fused (L-PBF) samples showed significantly finer γ' precipitates compared to laser powder directed energy deposited (LP-DED) ones.
4) The fully heat treated and machined L-PBF specimens exhibited 57% higher tensile strength compared to LP-DED ones, which was ascribed to the finer γ' precipitate size and smaller grain size.
5) Both L-PBF and LP-DED specimens exhibited similar ductility, which was attributed to a the same fracture mechanism involving carbide debonding from the matrix.

Acknowledgment

This research is partially supported by the National Aeronautics and Space Administration (NASA) under Cooperative Agreement No. 80MSFC19C0010. This paper describes objective technical results and analysis. Any subjective views or opinions that might be expressed in the paper do not necessarily represent the views of the NASA or the United States Government.

References

[1] R. Ghiaasiaan, N. Ahmad, P.R. Gradl, S. Shao, N. Shamsaei, Additively manufactured Haynes 282: effect of unimodal vs. bimodal γ′- microstructure on mechanical properties, Mater. Sci. Eng. A. 831 (2022) 142234.

[2] L.M. Pike, Development of a fabricable gamma-prime (γ′) strengthened superalloy, Proc. Int. Symp. Superalloys. (2008) 191–200.

[3] N. Ahmad, S. Shao, M. Seifi, N. Shamsaei, Additively manufactured IN718 in thin wall and narrow flow channel geometries: Effects of post-processing and wall thickness on tensile and fatigue behaviors, Addit. Manuf. 60 (2022) 103264.

[4] B. Blakey-Milner, P. Gradl, G. Snedden, M. Brooks, J. Pitot, E. Lopez, M. Leary, F. Berto, A. du Plessis, Metal additive manufacturing in aerospace: A review, Mater. Des. 209 (2021) 110008.

[5] L. Giorleo, E. Ceretti, C. Giardini, Ti surface laser polishing: Effect of laser path and assist gas, in: Procedia CIRP, 2015: pp. 446–451.

[6] R. Russell, D. Wells, J. Waller, B. Poorganji, E. Ott, T. Nakagawa, H. Sandoval, N. Shamsaei, M. Seifi, Qualification and certification of metal additive manufactured hardware for aerospace applications, Addit. Manuf. Aerosp. Ind. (2019) 33–66.

[7] N. Ahmad, R. Ghiaasiaan, P.R. Gradl, S. Shao, N. Shamsaei, Revealing deformation mechanisms in additively manufactured Alloy 718: Cryogenic to elevated temperatures, Mater. Sci. Eng. A. 849 (2022) 143528.

[8] A. Soltani-Tehrani, R. Shrestha, N. Phan, M. Seifi, N. Shamsaei, Establishing specimen property to part performance relationships for laser beam powder bed fusion additive manufacturing, Int. J. Fatigue. 151 (2021) 106384.

[9] I. Nandi, N. Shamsaeia, S. Shao, Investigating the effect of defects on the crack initiation of additively manufactured IN718 using crystal plasticity simulations, SFF 2022. (2022) 438–449.

[10] N. Ahmad, S. Baig, S. Reza Ghiaasiaan, P.R. Gradl, S. Shao, N. Shamsaei, Microstructure and mechanical properties of additively manufactured Inconel 718: A comparative study between L-PBF and LP-DED, (2022).

[11] M. Muhammad, R. Gusain, S. Reza Ghiaasiaan, P.R. Gradl, S. Shao, N. Shamsaei, Microstructure and mechanical properties of additively manufactured Haynes 230: A comparative study of L-PBF vs. LP-DED, 2022 Int. Solid Free. Fabr. Symp. (2022).

[12] A. Ramakrishnan, G.P. Dinda, Microstructure and mechanical properties of direct laser metal deposited Haynes 282 superalloy, Mater. Sci. Eng. A. 748 (2019) 347–356.

[13] K.A. Unocic, M.M. Kirka, E. Cakmak, D. Greeley, A.O. Okello, S. Dryepondt, Evaluation of additive electron beam melting of haynes 282 alloy, Mater. Sci. Eng. A. 772 (2020) 138607.

[14] I. Nandi, N. Ahmad, N. Shamsaei, S. Shao, Revealing texture induced abnormal tensile deformation behavior in additively manufactured Haynes 282 using crystal plasticity simulations, in: 2022: pp. 2271–2281.

[15] N. Ahmad, S. Reza Ghiaasiaan, P.R. Gradl, S. Shao, N. Shamsaei, Low cycle fatigue behavior of additively manufactured Haynes 282: Effect of post-processing and test temperature, 2023.

[16] ASTM E8, ASTM E8/E8M standard test methods for tension testing of metallic materials 1, Annu. B. ASTM Stand. 4. (2010) 1–27.

[17] A.E. Committee, E08, Standard Test Methods for Tension Testing of Metallic Materials, ASTM International, 2020.

[18] A. Mostafaei, C. Zhao, Y. He, S. Reza Ghiaasiaan, B. Shi, S. Shao, N. Shamsaei, Z. Wu, N. Kouraytem, T. Sun, J. Pauza, J. V. Gordon, B. Webler, N.D. Parab, M. Asherloo, Q. Guo, L. Chen, A.D. Rollett, Defects and anomalies in powder bed fusion metal additive manufacturing, Curr. Opin. Solid State Mater. Sci. 26 (2022) 100974.

[19] Y.Y. Sun, S. Gulizia, C.H. Oh, C. Doblin, Y.F. Yang, M. Qian, Manipulation and Characterization of a Novel Titanium Powder Precursor for Additive Manufacturing Applications, Jom. 67 (2015) 564–572.

[20] H. International, HAYNES ® 282 ® alloy, 2020.